

Invited review

Automated real-time formation evaluation from cuttings and drilling data analysis: State of the art

Harpreet Singh^{✉*}, Chengxi Li, Peng Cheng, Xunjie Wang, Ge Hao, Qing Liu

China National Petroleum Corporation USA, Houston, Texas 77042, USA

Keywords:

Drill cuttings
real-time
formation evaluation
industry 4.0
sustainability

Cited as:

Singh, H., Li, C., Cheng, P., Wang, X., Hao, G., Liu, Q. Automated real-time formation evaluation from cuttings and drilling data analysis: State of the art. *Advances in Geo-Energy Research*, 2023, 8(1): 19-36.
<https://doi.org/10.46690/ager.2023.04.03>

Abstract:

Traditional formation evaluation via laboratory testing and wireline logging of horizontal wells and deep formations face challenges due to several reasons and lead to uncertain results. Real-time cuttings and drilling data analysis of horizontal wells is an actively developing alternative approach to formation evaluation that can overcome several challenges faced by laboratory testing and wireline logging in providing improved estimates of formation parameters relevant to reservoir and completion quality. This study presents a state-of-the-art review of the latest methods and technologies in drill cuttings analysis to enable real-time characterization of the entire suite of formation properties, including chemical composition, densities and porosity, permeability, lithology, geomechanical properties, and characterization of fracture patterns. Specifically, the methods/techniques that enable characterizing drill cuttings in real-time and critically reviewed in this study include Raman spectroscopy for chemical composition, nuclear magnetic resonance for densities and porosity, liquid pressure pulse for permeability, deep learning for rock classification, 7 different methods for geomechanical properties, and mud loss signatures for characterization of fracture patterns. Benchmark comparison of drill cuttings analysis with the measurements from the core samples at similar depths is also reviewed. Key learnings are provided in 4 areas: to address the uncertainties in estimates of specific parameters affected by physical deformations due to drill bits, minimum cutting size for reliable nuclear magnetic resonance data, sweet spot identification, and power and network considerations for real-time analysis, respectively.

1. Introduction

The majority of new production wells in North America since 2012 have been horizontal, which now account for about 87% of the 14,832 total wells that started producing in 2022. In China, onshore oil and gas development is moving to unconventional shale and deep formations with horizontal wells in harsh conditions. With rapid development of unconventional horizontal wells where drilling and completion times continue to decrease with advancement of technology and its rapid implementation, such as fully remote smart drilling rigs and simultaneous fracturing, the advancements in formation evaluation are yet to see similar rapid implementation in the field. Typically, formation evaluation requires wireline logs and conducting time-consuming core-scale experiments to acquire parameters relevant to reservoir and completion (ge-

omechanical) quality. Acquiring laboratory-sized rock samples (~1 inch) from some target depths in shale reservoirs is challenging due to their relatively higher susceptibility to physical (e.g., delamination) and chemical instabilities that may change their actual in-situ properties, plus these samples are usually not recovered in horizontal drilling of the lateral. Further, wireline logging in deep formations (with high pressure and temperature) and mudrocks with horizontal wells faces several challenges (Yang et al., 2022). Therefore, traditional formation evaluation methods are generally inadequate to accurately capture the heterogeneity and anisotropy of unconventional shale resources and other deep formations.

Advancements in digitalization of oilfield assets and operations through 4th era (Industry 4.0) of digital technologies (e.g., cloud/edge computing, real-time data streaming, machine

learning, big data analytics, Internet of Things, etc.) has led to the development of innovative methods that can analyze drill cuttings and drilling data in real-time for rapid characterization of parameters relevant to reservoir and completion quality. Acquiring drill cuttings incurs no additional cost and they cover relatively larger depth of stratigraphic section. A significant advancement in formation evaluation is the real-time analysis of drill cuttings, which are retrieved along with drilling fluids at the surface before passing through shakers/vibrating machines to separate the cuttings from the drilling fluids and may be analyzed to estimate parameters relevant to reservoir and completion quality. Typically, each well-drilling operation produces tons of drill cuttings that are discarded, reinjected into the subsurface, buried in-situ, or placed in landfills (Martogi et al., 2019). Drill cuttings are an abundant source of data that covers a larger stratigraphic section in comparison to cores, and its analysis in near real-time enables relatively economical characterization of reservoirs, such as characterization of mineralogy, petrophysical properties, mechanical properties. Drill cuttings provide some unique advantages over other forms of data, which are its zero cost of acquisition and the relatively larger depth of stratigraphic section covered by drill cuttings. One of the main limitations to the use of drill cuttings for reservoir characterization is the presence of uncertainty in their tagged depths (Wittman et al., 2020; Singer et al., 2021), besides uncertainties in other parameters like porosity and density (Sanei et al., 2020). Although depth-matching is not required for the horizontal section of the well (Singer et al., 2021), depths of the drill cuttings in the vertical section of the wellbore are usually calibrated by comparing the properties measured from drill cuttings with their corresponding depth-calibrated measurements from well-logs. Further, one of the most promising measurements from drill cuttings are the mechanical properties of rocks, which are generally estimated from well-logs and/or laboratory measurements of core samples. Specifically, recent developments in small-scale testing (e.g., micro/nano indentation technique (Haftani et al., 2013; Glover et al., 2016; Dong and Chen, 2017) have enabled use of drill cuttings for rapid measurements of geomechanical properties of rocks that can be used in optimized placement of the horizontal lateral and in designing the hydraulic fracturing (HF) job. Particularly, two unique advantages of drill cuttings over core samples are continuous and rapid measurements (versus discrete and slow measurements from cores), whereas the advantage of drill cuttings analysis over well-logs is its low-cost. Further, the advancements in digitalization techniques and methods have theoretically enabled the near real-time use of drill cuttings in predicting formation properties, which is a new and actively developing area that can play an increasingly important role in cost-efficient drilling and completion of horizontal wells.

The rest of the paper is organized as follows. Section 2 provides a detailed description of the latest techniques, their novelty, limitations, and applications. Section 3 reviews the learnings about uncertainties in key parameters and data, sweet spot identification via trapped fluid analysis, and other considerations for real-time analysis. The final section provides a brief discussion related to the current situation, limitation, and

prospects... for real-time drill cuttings analysis.

2. Summary of technologies

Traditional analysis of drill cuttings involved three basic steps, which include: sample collection at shale shakers, cuttings cleaned of mud (drilling fluids) and dried, and crushed cuttings probed with X-ray fluorescence (XRF) for elemental composition, and X-ray diffraction (XRD) for mineralogy. The elemental composition is typically used to estimate synthetic GR-log from uranium (U), thorium (Th), potassium (K) obtained through XRF on cuttings. However, now it is not uncommon to acquire other supplementary measurements that are used for estimation of different parameters through various methods and techniques as summarized in Table 1, and discussed in detail ahead.

2.1 Chemical composition from raman spectroscopy

The use of Raman spectroscopy to characterize subsurface formations has become relatively more popular in the last decade (Truong-Lam et al., 2019; Katende et al., 2021) due to few major advantages over conventional optical microscopy as follows: ease of implementation, molecular sensitivity, non-destructive method, no sample drying required (unlike Infrared radiation spectroscopy), overcomes the limitations of wavelength dispersive X-ray fluorescence. These major advantages of Raman spectroscopy enable identifying precise composition of mineralogy at $< 1\mu\text{m}$ scales without any sample preparation as shown in Fig. 1. Raman spectroscopy measures the molecular vibrational frequency and the surface chemistry that also includes organic matter in rocks and gases, which is of significant importance in characterization of shale resources, for example, to determine the interactions of fluids and proppants with the rock (Katende et al., 2021).

2.2 Densities and porosity from nuclear magnetic resonance (NMR)

There is an increased interest in the value of NMR cutting analysis for formation evaluation particularly for horizontal wells that constrain the deployment of well-logging. NMR cutting analysis senses fluids in pore spaces and relies on the integrity of pore structure and the retention of fluids in the pore space (Mohnke et al., 2017; Althaus et al., 2019, 2020; Wittman et al., 2020; Singer et al., 2021).

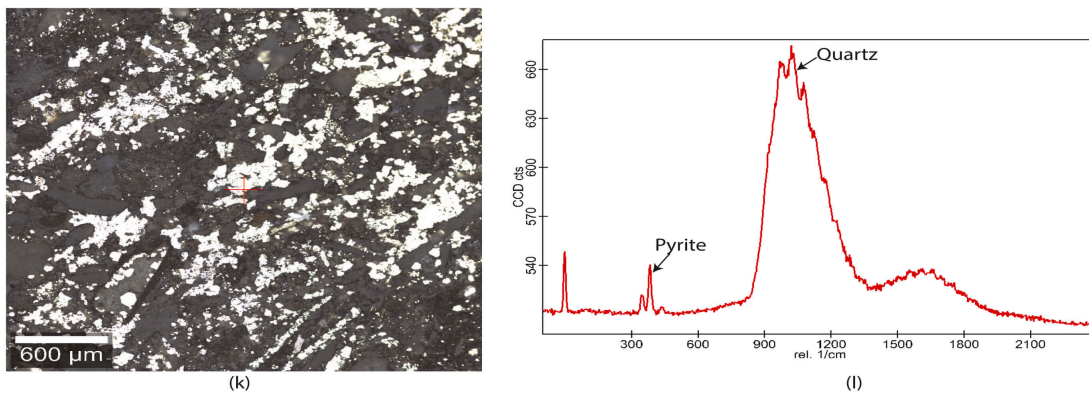
(1) Theory

Drill cuttings are usually of the size that is $\sim 0.5\text{-}3\text{ mm}$ with rough surfaces, such that the volume of fluid accumulated on the surfaces (e.g., due to contamination of drilling mud) of cuttings (V_l) can be similar to the volume of fluids present inside the rock cuttings (V_ϕ) as shown in Fig. 2.

The quantity and type of fluids present in a reservoir rock can be measured using low-field NMR (Althaus et al., 2020) that measures the spin-spin relaxation time (T_2), per Eq. (1), which enables identifying the fluid type and pore size. Therefore, accurate porosity measurement through NMR that works by sensing the fluids should ensure that the contribution of the surface fluids to the porosity are identified and eliminated;

Table 1. Summary of parameters, and their method of measurement, acquired using drill cuttings and drilling data.

Formation characteristic	Measured parameters	Data source	Method	Application
Chemical compositions	Elemental composition	Cuttings	XRF	Extensive
	Mineralogy	Cuttings	XRD	Extensive
			Raman spectroscopy	Novel
			TOC content	Cuttings
	Kerogen type, sample maturity	Cuttings	Rock-Eval pyrolysis	Extensive
Densities	Mineral and grain density maps	Cuttings	Automated petrography systems	Extensive
			DRIFTS for kerogen part only	Limited
			NMR	Extensive
Porosity, permeability	Porosities	Cuttings	DRIFTS (only kerogen porosity) NMR	Limited Extensive
	Permeability	Cuttings	Measurement at the well-site	Limited
Lithology	Rock type, lithology	Cuttings	DNN	Novel
Fluids	Trapped fluid analysis	Cuttings	Quadrapole mass spectrometry	Limited
	Geomechanics	Hardness and Young's modulus	Cuttings	Indentation
Poisson's ratio		Cuttings	IDSTD	Novel
Brittleness		Cuttings	Comprehensive brittleness index	-
UCS, BTS and SRN		Drilling	Multivariate regression	Novel
Dynamic Young's modulus		Drilling	ANN	Novel
Fractures	Sonic logs	Drilling	ANN	Novel
			Mud loss, SPP, TRQ, WOB, RPM	Drilling

**Fig. 1.** Identification of minerals in the Caney Shale samples using Raman spectroscopy (Katende et al. 2021).

this is usually achieved by identifying the large difference in the transverse relaxation times between the fluid on the rock surface versus the fluid inside the rock pores (Althaus et al., 2020). The transverse relaxation time of fluid in a rock sample (Eq. (1)) is the sum of the time due to pore surface relaxation, the time due to bulk relaxation, and the time due to heterogeneity in magnetic field (presence of gradient). For unconventional mudrocks with nanometer size pores, the time

due to pore surface relaxation (first term on the right hand side of Eq. (1); ρ_2 is surface relaxivity, and A is surface area) is the dominant contributor to the total relaxation time where the transverse relaxation time in such pores is ≤ 10 ms. However, bulk relaxation time (second term on the RHS of Eq. (1)) can be the dominant contributor to the total relaxation time if the cutting samples are not cleaned of the fluids on their surface.

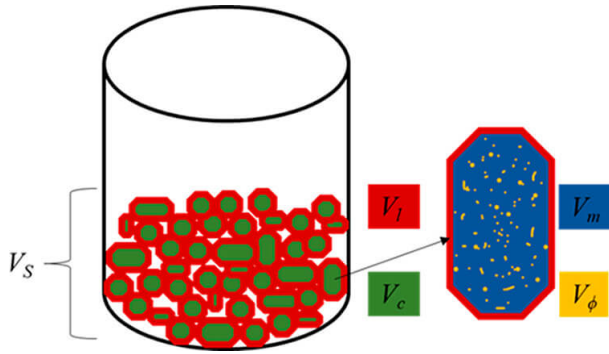


Fig. 2. Schematic illustrating volume of the cuttings (V_c), which is the sum of the solid matrix volume (V_m) and pore volume (V_ϕ), with the surrounding liquid volume (V_l) on the surfaces of the cuttings (Althaus et al., 2020).

$$\frac{1}{T_2} = \rho_2 \frac{A}{V_\phi} + \frac{1}{T_{2b}} + \frac{1}{T_{2D}} \quad (1)$$

where T_2 is transverse relaxation time; $\rho_2 A/V_\phi$ is pore surface relaxation; T_{2b} is bulk relaxation; T_{2D} is signal dephasing.

Using NMR measurements, V_ϕ and V_l can be obtained using the short relaxation peak and long relaxation peak, respectively, as shown by an example in Fig. 3.

Further, the mass of the cutting sample weighed in air and in the fluid are measured. These measurements are then used to obtain the bulk density, the matrix (grain) density, and the porosity of the cutting as follows:

$$\rho_b = \frac{m_a - V_l \rho_l}{V_c} \quad (2)$$

$$\rho_m = \frac{m_a - (V_\phi + V_l) \rho_l}{V_m} \quad (3)$$

$$\phi = \frac{V_\phi}{V_c} \quad (4)$$

where m_a is the mass of the cutting sample weighed in air; m_f is the mass of the cutting sample weighed in the fluid; ρ_b is the rock bulk density; ρ_m is the rock matrix (grain) density; ϕ is the rock porosity.

(2) Application

Uncleaned drill cuttings from unconventional oil-wet formation in the Middle East were used to measure the NMR T_2 relaxation time. To ensure repeatability of results from cutting analysis, two batches of samples (series 1 and series 2, respectively), were separated prior to cleaning. All the samples were then cleaned to remove the mud, which was done by mixing them with diesel and sieving through a 3 mm mesh and then through a 0.5 mm mesh to separate the cuttings from mud solids (< 0.5 mm) and cavings (> 3 mm), followed by cleaning with the diesel (for water-wet formation, water would be a better choice as a fluid for saturation). Further, the cleaned samples were used to measure the T_2 relaxation times, where the processed T_2 spectrum along and the cumulative volume are shown in Fig. 3. The run time to perform measurement for each sample was approximately 2 minutes, which when performed at the well site would mimic near real-time. The optimum T_2 cutoff for this specific was determined to be 44 ms, such that a relaxation time ≥ 44 ms is identified as the bulk fluid and < 44 ms is identified as pore fluid. The optimum

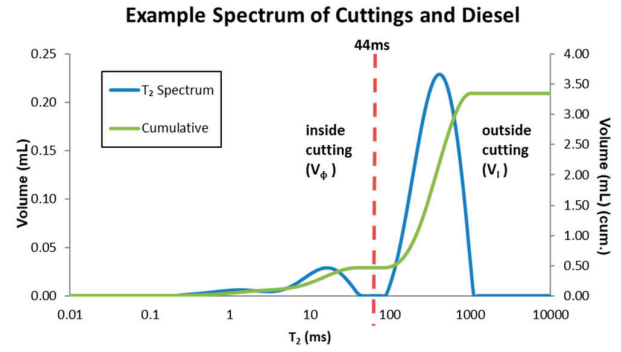


Fig. 3. An example illustrating the measurement of pore volume and surrounding liquid volume from drill cutting based on the NMR measurement (Althaus et al., 2020).

T_2 cutoff for each formation may vary as it is affected by the pore size, wettability, and mineral content (Althaus et al., 2020).

Following NMR measurements, two different masses of each sample (and sample cup) are acquired sequentially as follows: mass in air, and mass after immersing in diesel. The sample cup must also be cleaned and then weighed, both in and out of diesel. Later, the cutting samples were dried and measured using NMR, with the results for the diesel-saturated and dried samples shown in Fig. A-1, where the smaller (fast relaxing) peak is likely an effect of bitumen. The NMR-based measurements were used to estimate bulk density, matrix density, and porosity, per Eqs. (2), (3), and (4), respectively, as shown in Fig. A-2, which exhibit high reproducibility in all the three measured parameters. Between the measured values of bulk density, matrix density, and porosity for the two batches, porosity shows the largest variation, possibly due to stresses exerted by the drill bits during drilling that deforms the pore space in the cuttings through induced micro-fractures.

2.3 Permeability measurement using liquid pressure pulse

Permeability is typically estimated using empirical correlations that relate permeability with pore size distribution, and their connectivity, which are measured using one of the following techniques: mercury porosimetry, NMR, or image analysis.

(1) Theory

An alternative method that can directly measure the permeability of drill cuttings without any specific laboratory conditioning (Egermann et al., 2002) involves using about 100 cm^3 of cuttings, a pressure vessel, and viscous oil; specifically, the cuttings are placed in the pressure vessel and the cell is then filled with the viscous oil such that the invasion of oil into the cuttings traps a certain amount of gas as shown in Fig. 4. The fundamental idea behind this experiment is to develop an effective flow inside the cuttings by injecting a viscous liquid that compresses the residual gas contained within the cutting; the viscous liquid helps slow down the pressure decrease inside the rock. The experimental procedure involves two sequential stages, which are a very short period of constant injection rate, and a longer period of constant

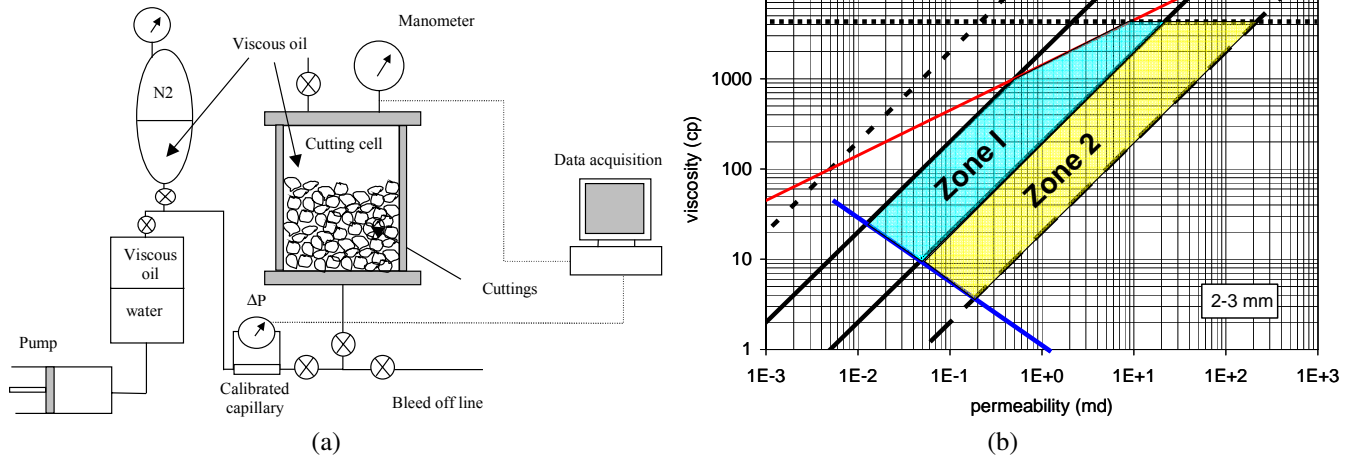


Fig. 4. (a) Schematic of the experimental setup for measuring the permeability of drill cuttings, (b) abacus to guide the selection of viscosity of the injected liquid.

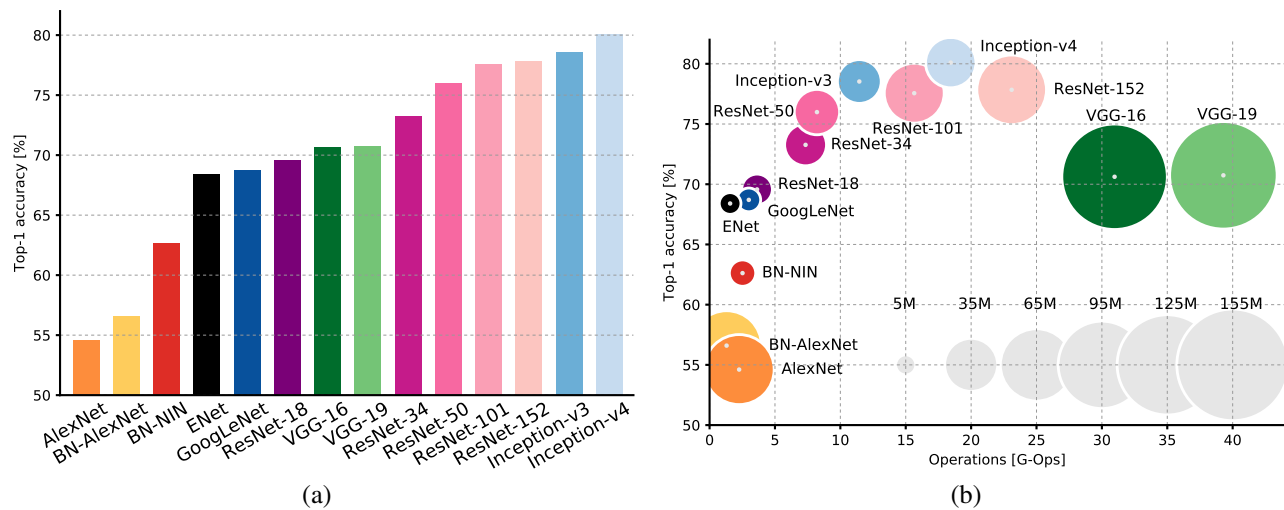


Fig. 5. Accuracy of various DNNs since AlexNet's breakthrough with Inception-v4 as the best performer (Canziani et al., 2017).

injection pressure. The permeability of the drill cuttings using the setup shown in Fig. 4 is calculated numerically through a simple model (given in Appendix) that describes the flow of a viscous liquid into a compressible medium of spherical geometry, which is similar to a well test, except that the oil and reservoir compressibilities are replaced by the trapped gas (Egermann et al., 2002; Lenormand and Fonta, 2007).

(2) Application

One application is the total volume of oil injected into the cuttings (chalk sample with porosity of 0.35) cell with time, where the permeability obtained by fitting the beginning of the curve (since the largest pores control the permeability) is 0.3 mD (Fig. A-4(a)). Another example with a carbonate sample (porosity of 0.23) and pure glycerol (viscosity around 1200 cp), where the permeability obtained by fitting the beginning of the curve is 5 mD (Fig. A-4(b)).

2.4 Machine learning-based classification of lithologies and rock types

Although some machine learning (ML)-based rock identification on thin sections of cuttings and drill cuttings have been previously proposed that use deep convolution neural network (CNN) (Cheng and Guo, 2017, Kathrada and Adillah, 2019), these studies classify each image of cuttings with only one class of rock type (the most dominant) and are not suitable for analysis of cutting mixtures in real drilling environment where rock types show transition in lithologies during drilling. Specifically, one of the important applications of drill cuttings includes interpreting lithology by reconstructing and reordering geological layers, which requires interpreting variations in intra-class and inter-class of rock types. This is an important requirement because different cuttings with similar color and grain size can be of different rock types as shown in Figure 5a, and multiple rock types can be present in the same sample.

(1) Theory

Deep learning models that take cutting images as input and provide output in terms of the cutting size and rock type at a pixel-level can enable classifying the intra-class and inter-class variation in particle size and rock types within a single image of drill cutting, where the proportion of each rock type would be the proportion of pixels in the image (Tamaazousti et al., 2020; Di Santo et al., 2022; Ismailova et al., 2022; Yamada and Di Santo, 2022). Such a pixel-level identification approach also naturally enables predicting the size, shape, and variation in colors of different rock types within the same image.

Deep Learning Models. AlexNet was the first deep neural network (DNN) in 2012 used in the *ImageNet* dataset problem in the field of computer vision, and since then several other DNNs have been introduced with improved accuracy (Canziani et al., 2017), as shown in Fig. 5(a). Fig. 5(b) shows accuracy as a function of computational cost and number of parameters in each network, which suggests that the versions of the Inception models with the highest accuracy are possibly near an inflection point on the ImageNet dataset. In other words, Inception-v4 DNN is close to the point in terms of accuracy and computational costs that any further improvement in accuracy is outweighed by the added complexity in the model.

The DNNs shown in Fig. 5 are essentially CNNs with varying number of layers. A CNN is well-suited to process 2-dimensional data like images and it does not require selecting features to classify the images. A CNN architecture is composed of multiple layers of neurons in the form of convolutional and pooling layers. The two basic steps involved in CNN include convolution on the input data (e.g., image) using filters to get convolved feature, which is passed on to the pooling layer for down-sampling operation.

Current computer vision DNNs have greater than 90% accuracy in image classification, and take minutes to train on parallel GPUs, compared to the time it used to take (six days with 2 parallel GPUs) when AlexNet was introduced.

(2) Application

The architecture of DNN-based classification shown in Fig. A-5 (Tamaazousti et al., 2020) was trained and tested using a suite of 300 pictures of cuttings samples that were standardized in terms of the same camera, support tray (background), and distance from camera to tray. The cutting samples contained three rock types (carbonate, sandstone, and shale) from different geographies, including dry and wet cuttings, single and mixed rock types. Further, the 300 pictures used for training and testing the model were separated into three scenarios, which were dry single lithologies (240 images), dry mixtures (50 images), and wet mixtures (10 images). Out of these 300 images, the model was trained using 200 images that contained only single lithology cuttings samples, whereas the remaining images were used for testing.

One of the primary reasons the model was trained using images with single lithology was to avoid the precise segmentation in rock boundary (pixel-level) that would be required in images with multiple lithologies, which is not only time consuming, but the segmentation provided by a human eye may not resolve the precision required for the deep learning-based training. Therefore, training the model required labeling

each image with only single rock type present in pixels of the image, i.e., one binary mask per entire image. Further, pre-processing of the images prior to assigning the segmentation labels of rock type required removing the background from the cutting images that was achieved using a simple image-processing algorithm.

Learning a model directly with a single class of rock type in each image, out of three classes of rock types, does not lead to an accurate model due to wide variations in the testing images that contain intra- and inter-class of rock types. Therefore, to improve the model prediction, labeling for each of the three classes was refined to include sub-classes (grain size, color, etc.), referred as meta-class, in a hierarchical manner based on visual appearance that finally leads to 72 sub-classes as shown by the workflow in Fig. A-5.

The ResNet model pre-trained on ImageNet dataset was used and adapted for segmentation tasks for drill cuttings images. Fig. A-6 shows the results of the trained model when applied on blind images of cuttings that contained mixture of lithologies, where the top two rows contain cuttings from sandstone and carbonate lithologies, whereas the last row contains all the three lithologies.

The second application of ML-based classification is Equinor in-house tool called Cuillin (Cuttings Image Lithology Interpretation with Neural-Networks) (Equinor, 2019) that uses ML to classify and label images of rock cuttings without manual intervention. Cuillin is developed using Inception-v3 as the DNN, as shown in Fig. A-7a, which was trained for this particular task using offshore dataset from Norway and UK. The key steps in deep learning of Cuillin include the following:

- a) Splitting the data into training and test set at the well-level.
- b) Assigning lithology (labels) for each training image, and discarding the ambiguous images.
- c) Making 45 sub-crops per an image.
- d) Using PyTorch framework to train Inception-v3 DNN architecture to distinguish between ~15 lithology classes.

The total time taken for data processing and DNN training (with ~0.85 F1 score in ~25 epochs) of Cuillin was ~7 hours on 4×V100 GPU AWS node (Equinor, 2019). Cuillin can predict lithology distribution for a typical well with 5001-1000 images in ~2-4 minutes (Equinor, 2019) and can be deployed in low-power embedded systems.

An example of the multi-class lithology classification and visualization of DNN predictions using Cuillin (Fig. A-7b), which is also assisted by visualizations of the DNN's working mechanism.

The third application of ML-based classification is R-CNN architecture-based model (Yamada and Di Santo, 2022) that provides formation top detection, and lithology classification based on cutting size/shape identification as shown in Fig. A-8. The digital microscope used in capturing the photographs of cuttings was calibrated for absolute distance measurements to have the exact pixel size (Di Santo et al., 2022), which together with calibrated measurements were then used to develop this model. This ML model also allows classifying grainy textured

object, extracting and measuring the size, shape, and color of each grain, and separating it from the background (Fig. A-8a). The ML model also performs particle clustering differentiating lithologies based on multi-dimensional mathematical space in the form of color intensity, color hue and texture homogeneity (Fig. A-8b).

2.5 Geomechanical properties from drill cuttings

2.5.1 Diffuse reflectance infrared fourier transform spectroscopy (DRIFTS) method

(1) Theory

DRIFTS measurements (Prioul et al., 2018) include weight fractions of 9 inorganic mineral components (smectite, illite, kaolinite, chlorite, quartz-feldspar, muscovite, calcite, dolomite, and anhydrite; however, only major 6 of them are used in analysis by clubbing the four clays together as clay, and quartz, feldspar, muscovite together as qfm, as shown by Table A-1 in Appendix), and organic matter that is only kerogen (because drill cuttings cleaned with solvents remove the soluble organics). The density of the combined inorganic (mineral) and organic phases is estimated using the weight fractions and the known densities of the minerals and the kerogen as follows:

$$\frac{1}{\rho_{mo}^{drifts}} = \frac{W_{ker}}{\rho_{ker}} + \sum_i \frac{W_{mo,i}}{\rho_i} \quad (5)$$

where W_{ker}/ρ_{ker} is organic matter, $\sum_i W_{mo,i}/\rho_i$ is inorganic matter.

DRIFTS model assume that the drill cuttings samples are organic-rich shale, strongly anisotropic, and transversely isotropic layered medium with an axis of symmetry perpendicular to the bedding layers.

DRIFTS technique measures only kerogen part of the organic matter components, which means it does not measure the hydrocarbon and bitumen parts. To be able to obtain the missing data for the non-kerogen part (hydrocarbon, bitumen, and water) in the formation, the DRIFTS technique uses empirical petrophysical model that is calibrated using the volume fractions from well-logs and it is related to the DRIFTS by applying a correction factor (ω_c) as follows: $W_{tom}^{log} = \omega_c W_{tom}^{drifts}$, where $\omega_c \geq 1$.

The petrophysical volumetric models assumes 3 volumetric (1 phase for water and 2 phases for solid/matrix) phases as follows:

- a) Brine/water phase: with associated volume as ϕ_w .
- b) Solid/matrix phase: with associated volume as $(1 - \phi_w)$ and composed of following:
 - i) Mineral or inorganic phase: composed of 6 major minerals shown in Table A-1 associated with corresponding volumes $\phi_{m,i}$.
 - ii) Organic matter phase: composed of kerogen, hydrocarbon, and bitumen with associated volume as $\phi_{tom} (= \phi_{ker} + \phi_{hyd} + \phi_{bit})$. For low-maturity, oil-bearing reservoirs, a single organic matter phase (with its volume depicted as ϕ_{tom}) is reasonable because of sufficiency small contrast in bulk densities and elastic properties of kerogen, hydrocarbon, and bitumen.

The procedure to estimate the geomechanical model from drill cuttings includes two steps, which are summarized on a flowchart shown in Fig. A-9.

(2) Application

This case study involves estimation of in-situ stress using cutting-based measurements and the data used come from two vertical pilot wells (drilled through the Quintuco and Vaca Muerta Formations in the Neuquén Basin, Argentina), and one horizontal lateral well in the Vaca Muerta Formation. Drill cuttings measurements along with a comprehensive logging suite, cores, and in situ stress tests, from a vertical control well were used to define and calibrate four models: petrophysical, rock physics, dynamic-static elastic, and geomechanical. Dynamic anisotropic elastic moduli are calculated using the rock-physics model, whereas static elastic properties and the minimum stress are calculated using the dynamic-static and geomechanics models. DRIFTS data from cuttings in the target lateral well are used to calculate stresses, which is verified by accurate reconstruction of sonic-log-derived elastic moduli, as shown in Fig. A-10.

A major observation relevant to well completion optimization is that the elastic-property heterogeneity in these wells can be solely explained on the basis of variations in mineralogy and total organic matter (TOM), as shown in Fig. A-11. Specifically, with the increase in TOM plus clay content, the horizontal and vertical Young's moduli (E_H and E_V) decrease, but elastic anisotropy (E_H/E_V) increases and a cumulative decrease in minimum horizontal stress (σ_h); if the calcite content increases, the opposite trend holds, i.e., E_H and E_V increase, but elastic anisotropy (E_H/E_V) decreases and a cumulative increase in σ_h . The variation in minimum stress estimated using the above method can be used as an input to optimize HF job design.

2.5.2 Micro/Nano indentation method

(1) Theory

Recent advancements in small-scale testing enable mechanical testing on drill cuttings that can provide measurements from nanoscale (load < 100 mN) to microscale levels (load < 15 N) (Martogi et al., 2019; Shi et al., 2020; Alipour et al., 2021; Esatyana et al., 2021; Katende et al., 2021). Indentation measurements at the nanoscale-level enable acquiring mechanical properties of different constituent phases, and measurements at the microscale-level enable acquiring the bulk mechanical properties of the composite behavior of all constituent phases present at the nanoscale-level. The indentation measurements on shale samples require the following 3 steps:

- 1) The table on which indentation is performed is vibration-proof by pressurizing it to about 20 psi to prevent imperfections during the test.
- 2) This is followed by calibrating the vickers diamond indenter tip using a steel block. This calibration ensures that the elastic modulus and hardness measured during indentation are comparable to the ideal values of steel.
- 3) Indentation test is performed in three sequential steps: indenting the sample to a maximum load, holding the

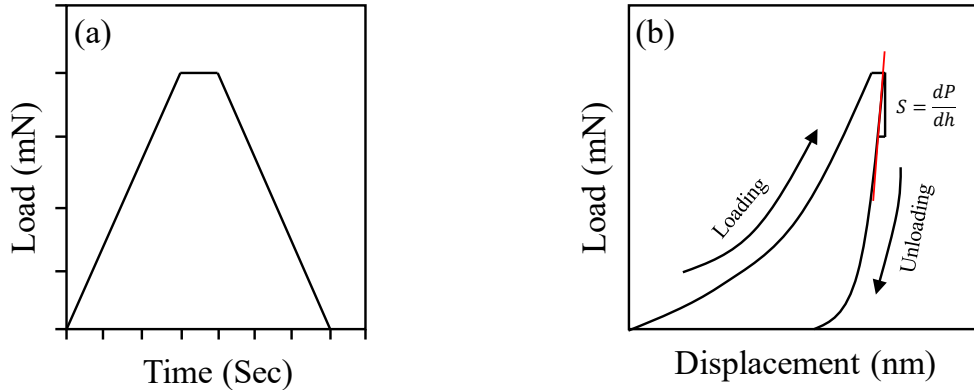


Fig. 6. (a) General loading/unloading sequence for indentation tests, which include loading the sample, holding, and unloading the sample, (b) a conceptual plot depicting indentation process with load versus displacement curve, where P is the load (force) that is referred as F (in place of P) in the provided derivation, and displacement is referred as h (Martogi et al., 2019).

load for ten seconds, and removing the load progressively (Fig. 6). Both the loading and unloading sequence was performed at a constant loading rate.

The two elastic mechanical properties obtained from the load vs. displacement (depth) plot shown in Fig. 6 are: indentation modulus and hardness. The hardness (H) of the cuttings is measured using (Katende et al., 2021):

$$H = \frac{F_{\max}}{A_c} \quad (6)$$

where F_{\max} is the maximum load applied, and A_c is defined as follows:

$$A_c = 24.5 \times \left(h_{\max} - \frac{3F_{\max}}{4 \left(\frac{dF}{dh} \right)_{at \max h}} \right)^2 \quad (7)$$

Indentation depths (h) are measured using laser surface profilometer linked to the Raman microscope. The Young's modulus of the cuttings is measured as follows:

$$E = \frac{(1 - \nu^2)E_r E_i}{E_i - (1 - \nu_i^2)E_r} \quad (8)$$

$$E_r = \frac{S\sqrt{\pi}}{2\sqrt{A_c}} \quad (9)$$

where E_i is the Young's modulus of the indenter (e.g., diamond; 1,140 GPa for Berkovich indenter), ν_i is the Poisson's ratio of the indenter (e.g., diamond; 0.07 for Berkovich indenter), ν is the sample Poisson's ratio, E_r is the reduced modulus.

(2) Instrumentation

An illustration of instrumentation required to perform indentation tests on a rock cutting, and the experimental preparation required for indentation, are shown in Fig. 7.

(3) Application

The study uses indentation along with Raman spectroscopy on drill cuttings from Caney shale formation (an organic-rich play in Oklahoma) to measure their geomechanical properties that are validated using a numerical model of the experiment (Fig. A-12). The modeling results for these samples, show that

proppant embedment, which significantly reduces a fracture's aperture, can vary significantly within a fracture, especially in weaker formations. Propellant embedment can be limited through close proppant packing per the results in Fig. A-12. Some of the observations depicted that can be used to optimize the completion are as follows:

- 1) Plastic deformation and plastic strength properties for proppant embedment can accurately describe the localized shale failure just below the proppant-shale contact.
- 2) Low hardness and elastic modulus imply zones susceptible to proppant embedment.
- 3) Smaller indents imply higher hardness and elastic modulus.
- 4) Higher clay contents reported least hardness and elastic modulus.
- 5) Variation in composition of the rock fabric impact the degree of proppant embedment along the surface of the same material.
- 6) Axial and radial cracks can dominate for indentation on samples cored at 45° to the bedding planes.

2.5.3 Inclined direct shear testing device (IDSTD)

(1) Theory and instrumentation

IDSTD enables mechanical properties characterization under variable confining pressure with drill cuttings, where the volume of material required is as small as 2.3 cm^3 (Abousleiman et al., 2007, 2010), which is close to penny-shape samples ($\sim 20 \text{ mm}$ diameter and 7 mm thickness). IDSTD setup, measures acoustic velocities (V_{P90} , V_{S90}), which enable estimation of Young's modulus and Poisson's ratio as follows (Abousleiman et al., 2010):

$$\rho V_{P90}^2 = \frac{E(1 - \nu)}{(1 + \nu)(1 - 2\nu)} \quad (10)$$

$$\rho V_{S90}^2 = \frac{E}{2(1 + \nu)} \quad (11)$$

Due to the small IDSTD sample size, only three acoustic measurements are possible during loading, namely V_{P90} , V_{S90} , and $V_{P\theta}$.

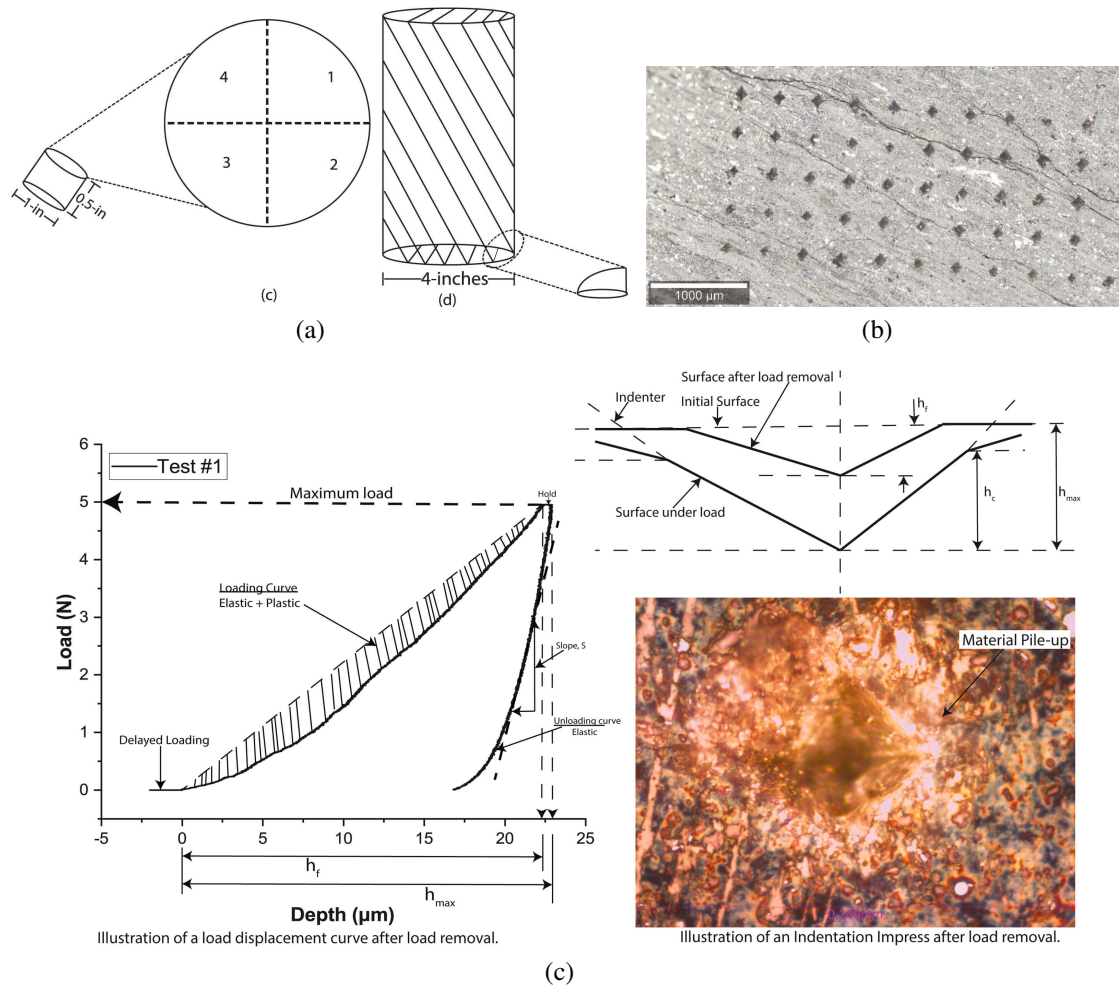


Fig. 7. (a) Schematic illustrating the planned design and execution of indentation, (b) illustration of the final surface after indentation obtained using Raman Surface Profilometry discussed in Section 2, (c) illustration depicting the load versus displacement curve during indentation and the indentation impress after removing the load (Katende et al., 2021).

(2) Application

Shale samples from Middle Woodford in Oklahoma were used to estimate compressive strength in contact with different oil-based muds. Acoustic measurements were used during confinement and deviatoric loading to monitor the changes in anisotropic dynamic stiffness coefficients (C_{ij}) and Biot's pore pressure coefficients (α_{ij}) (Abousleiman et al., 2010). The dynamic elastic and poroelastic properties were measured by acoustics (sonic velocities) under both confining pressure and deviatoric stress. The anisotropy ratio of P- and S-wave during hydrostatic confinement and deviatoric loading are given by the variation in Thomsen's coefficients ε ($(C_{11} - C_{33})/2C_{33}$) and γ ($(C_{66} - C_{44})/2C_{44}$), as shown in Fig. A-13. An initial increase in ε and γ during deviatoric loading at 13.79 MPa confining pressure might be due to formation of micro-cracks parallel to the bedding planes or the shale fabric, whereas the decrease in their values during confinement is likely due to closure of preexisting micro-cracks in the sample.

2.5.4 Comprehensive brittleness based on mechanical and mineral properties

(1) Theory

A comprehensive brittleness model that includes the effect of mineral brittleness and mechanical brittleness (Shi et al., 2020) enables reliable estimations of the homogenized Young's modulus and Poisson's ratio by the integration of nano-indentation method with the deconvolution technique, whereas mineral compositions of the indentation area are obtained using energy dispersive spectrometer (EDS) (Shi et al., 2020).

(a) Young's modulus and Poisson's ratio from indentation technique

The model to predict Young's modulus and Poisson's ratio of the drill cutting sample using indentation technique is given by Eq. (6) through Eq. (9).

(b) Deconvolution technique

The deconvolution technique provides an experimental cumulative distribution functions (CDF) of the mechanical properties, including hardness, modulus, and creep viscoelastic

properties. The CDF of a mechanical parameter (X) measured at various gridded-locations (i) on the cuttings sample through indentation technique is developed as follows:

$$D_X(X_i) = \frac{i}{N} - \frac{i}{2N}, \text{ for } i = 1, \dots, N \quad (12)$$

The corresponding probability density function (PDF) of the mechanical property for phase J , $P_J(x)$, measured using indentation is typically given using a Gaussian mixture model (Shi et al., 2020) (with μ_J and S_J as the mean and standard deviation of the phase J , respectively) as follows:

$$P_J(x) = \frac{1}{\sqrt{2\pi S_J^2}} \exp\left(-\frac{(x - \mu_J)^2}{2S_J^2}\right) \quad (13)$$

The unknown parameters of theoretical PDF are estimated by fitting it over the experimental CDF and optimizing their difference with $\mu_X^j + S_X^j < \mu_X^{j+1} - S_X^{j+1}$, $j = 1, \dots, n - 1$ as follows (the number of phases, n , is an assumed parameter):

$$\sum_{k=1}^N \sum_X \left(D_X(X_i) - \sum_{j=1}^n f_j P_J(x) \right)^2 \quad (14)$$

Eq. (14) enables predicting mechanical properties of each phase in the cuttings sample, and relative volume fraction of each phase, which are then used to determine homogeneous mechanical properties.

(c) Homogenization method (Scale-up)

Homogenization method is a technique to scale-up small-scale predictions to macro-scale that is self-consistent. Specifically, the particular model used for homogenization is a multi-scale multi-component model by Mori-Tanaka (Shi et al., 2020) to predict homogenized isotropic bulk modulus (K_h) and shear modulus (G_h) composed of 3 phase (with μ_r , k_r as the shear moduli and bulk moduli of each phase $r = 0, 1, 2$ with f_r as their corresponding volumetric fraction; μ_0 , k_0 as the shear moduli and bulk moduli of reference matrix) as follows:

$$K_h = \frac{\sum_{r=0} \frac{f_r k_r}{3k_r + 4\mu_0}}{\sum_{r=0} \frac{f_s}{3k_s + 4\mu_0}} \quad (15)$$

$$G_h = \frac{\sum_{r=0} \frac{f_r \mu_r}{\mu_0(9k_0 + 8\mu_0) + 6\mu_r(k_0 + 2\mu_0)}}{\sum_{s=0} \frac{f_s}{\mu_0(9k_0 + 8\mu_0) + 6\mu_s(k_0 + 2\mu_0)}} \quad (16)$$

Using Eqs. (15) and (16), the homogenized Young's modulus (E_h) and Poisson's ratio (ν_h) of shale are calculated as follows, respectively:

$$E_h = \frac{9K_h G_h}{G_h + 3K_h} \quad (17)$$

$$\nu_h = \frac{3K_h - 2G_h}{2G_h + 6K_h} \quad (18)$$

(d) Comprehensive brittleness model

The comprehensive brittleness model is developed using the mineral-based and mechanical-based brittleness, where the mineral-based brittleness (B_1) is calculated using quartz, clay, and carbonate components, as follows (Shi et al., 2020):

$$B_{n1} = \frac{W_{qt}}{W_{qt} + W_{cal} + W_c} \quad (19)$$

Young's modulus and Poisson's ratio are typically used to calculate brittleness as these parameters can be generally obtained from laboratory experiments or well-logs. However, for the drill cuttings, homogenized values of Young's modulus and Poisson's ratio are derived through deconvolution technique and homogenization method based on nano-indentation measurements, which are used to calculate mechanical-based brittleness (B_2) as follows (Shi et al., 2020):

$$B_{n2} = \frac{E_{nh} + \nu_{nh}}{2} \quad (20)$$

where E_{nh} and ν_{nh} are the normalized values of the E_h and ν_h distributions, respectively, which are calculated as follows:

$$E_{nh} = \frac{E_h - E_{h,\min}}{E_{h,\max} - E_{h,\min}} \quad (21)$$

$$\nu_{nh} = \frac{\nu_h - \nu_{h,\min}}{\nu_{h,\max} - \nu_{h,\min}} \quad (22)$$

The comprehensive brittleness (B_c) is simply the mean of the mineral-based brittleness and mechanical-based brittleness parameter as follows:

$$B_c = \frac{B_{n1} + B_{n2}}{2} \quad (23)$$

(2) Application

The method is applied to estimate the brittleness of a shale gas well in Lower Silurian Longmaxi Formation (China) where 15 to 19 drill cuttings were used for nanoindentation tests and to measure comprehensive brittleness parameter for each well. Mineral distribution on gridded area for indentation tests was interpreted using a combination of EDS and backscattered electron images from SEM, as shown in Fig. A-14(a), which are used to correlate with the mechanical properties shown in and Fig. A-14(b). Results in Fig. A-14(c) show three different peak values that correspond to 3 different phases in the sample, which are used to divide all the nano-indentation sites into 3 groups: i) G1, which includes the softest indentations, ii) G3, which includes the hardest indentations, and iii) G2, which includes the remainder. Using Eqs. (17) and (18), homogenized Young's modulus and Poisson's ratio can be estimated for indentation measurements from all cuttings, which vary from 14.21 to 22.1 GPa (with an average of 19.72GPa), and from 0.18 to 0.26 (with an average of 0.22), respectively. Similarly, mineral-based Young's moduli and Poisson's ratio of the 3 identified phases (G1, G2, G3) are approximately 25, 43, and 97 GPa, and 0.3, 0.25 and 0.25, respectively.

Therefore, the mechanical-based and mineral-based brittleness values from all the samples (averaged values of 0.51 and 0.47, respectively) are used to calculate the comprehensive brittleness values per Eq. (23) and plotted versus the depth as shown in the last track of Fig. A-15. The last track in Fig. A-15 shows two intervals (1 and 2) with relatively larger brittleness values that can be target for HF, however, interval 1 was selected for HF due to its higher gas potential.

Pressure versus time data from HF treatment for one stage of a horizontal well drilled along interval 1 had the largest B_c

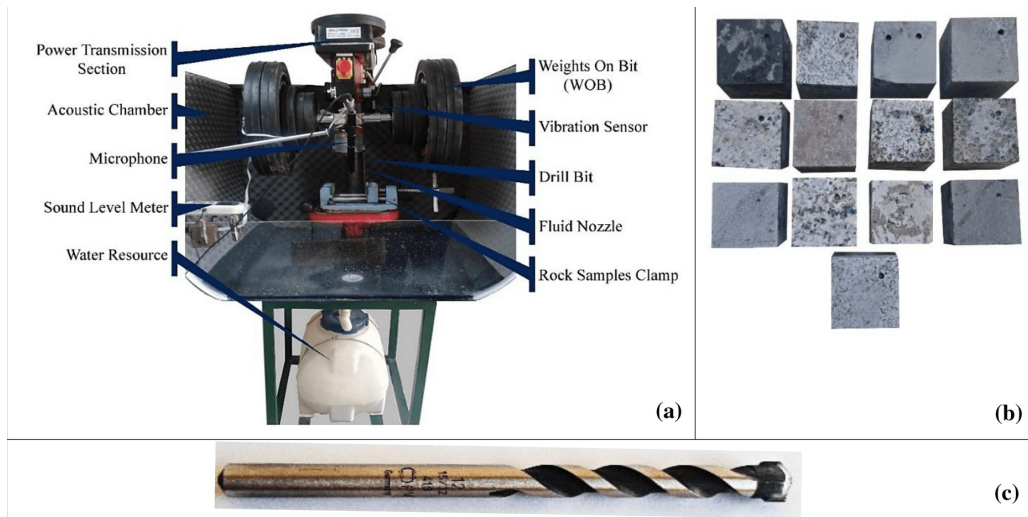


Fig. 8. (a) Laboratory-scale rotary drilling machine and its labeled components, (b) igneous rock samples, (c) drill bit (Khoshouei and Bagherpour, 2021).

(Fig. A-16). The fracturing-treatment pressure dropped sharply to fracture-closure pressure when the fracturing pump (blue colored legend) stopped (zero rate), such that this similar sharp drop was exhibited in fracturing treatment of all other stages of this well, indicating formation of complex fracture network in this interval. The higher value of comprehensive brittleness for this interval was verified and supported by the gas production rate from i) this well (Fig. A-16) that was much higher ($34.3 \times 10^4 \text{ m}^3$ per day) than the other wells, and ii) two other wells with similar comprehensive brittleness were also relatively high ($11.2 \times 10^4 \text{ m}^3$ per day) than the other wells.

2.5.5 Using drilling data

Although some tools/techniques enable predicting geomechanical properties at the well-site, these tools only sense organic matter (e.g., DRIFTS Method), so the predicted values lack robustness due to simplified assumptions in the underlying rock physics models used for prediction. In this respect, predicting geomechanical properties via statistical and machine learning regression of the drilling data is helpful as it allows overcoming the assumptions and constraints of the rock physics models. The variation in drilling parameters used in the regression analysis directly captures the effect of the underlying chemical compositions.

(1) Estimating formation strength parameters

(a) Theory and instrumentation

Acoustic and vibration signals propagated during the drilling process, using the instrument and sample shown in Fig. 8, were found to statistically correlate with uniaxial compressive strength (UCS), brazilian tensile strength (BTS) and schmidt rebound number (SRN) (Khoshouei and Bagherpour, 2021). Specifically, UCS, BTS, and SRN were predicted through multivariable regression by using Sound Pressure Level (SPL), First Dominant Frequency (FDF), and Vibration Level (VL), respectively, as the predictor variables.

(b) Application

To predict the physical and mechanical properties based on the proposed approach, 13 samples of igneous rock each with $9 \text{ cm} \times 9 \text{ cm} \times 9 \text{ cm}$ dimension were used and fixed by a special clamp prior to the drilling operation. The operating conditions of the drilling tests, such as diameter of the drill bit, the thrust force or weight on bit (WOB), the cooling fluid rate, the speed of the drill bit, etc., are described in Table A-3.

SPL, FDF, and VL were obtained during the drilling tests. Multivariable regression of the sound pressure level (dB), the dominant frequency (Hz), and vibration level (m/s^2) were used to obtain the mechanical properties of the rocks, i.e., UCS ($R^2 = 0.92$), BTS ($R^2 = 0.81$), and Schmidt hardness ($R^2 = 0.83$). The mechanical properties of the rock samples obtained using this approach, as shown in Fig. A-17, are consistent with the measured values and verifies the accuracy of the method.

(2) Estimating dynamic Young's modulus

(a) Theory

Static Young's modulus value is an important parameter in hydraulic fracturing design, which is obtained using the dynamic Young's modulus (E_{dyn}) based on one of the several empirical correlations applicable to specific rock types. The E_{dyn} is typically estimated by analyzing the compressional velocity (V_P), shear velocity (V_S), and bulk density (ρ) per Eq. (24), where these three parameters are obtained using wireline logs and may not be available for all the formations readily (Mahmoud et al., 2021):

$$E_{dyn} = \frac{\rho V_S^2 (3V_P^2 - 4V_S^2)}{V_P^2 - V_S^2} \quad (24)$$

An optimized artificial neural network (ANN) trained using drilling parameters from different three well located in the same field in the Middle East was shown to predict E_{dyn} accurately with an error of less than 4% in all the tested wells (Mahmoud et al., 2021).

(b) Application

The ANN model was trained using the following 6 drilling parameters: rate of penetration (ROP), WOB, stand-pipe pres-

sure (SPP), torque (TRQ), drilling mud flowrate, and the DSR.

The trained ANN model (with $n = 6$ input features and single hidden layer with $m = 25$ neurons) was represented in the form of a mathematical function based on its weights (w), transfer function (tangent-sigmoid function), and biases (b) as follows (Mahmoud et al., 2021):

$$E_{dyn} = \sum_{j=1}^{m=25} w_{j1} \sum_{i=1}^{n=6} \frac{1}{1 + e^{-w_{ij}x_i + b_j}} \quad (25)$$

The numerical values of the weights and biases of the optimized ANN depicted by Eq. (25) are provided in Table A-4. The ANN model was trained using 2,054 data samples from Well-A (Fig. A-18), followed by its testing using 871 data samples from Well-B (Fig. A-19), and validation using 2,912 data samples from Well-C (Fig. A-20). The average absolute percentage error of the E_{dyn} estimated using the optimized ANN model for the training, testing, and validation datasets were 3.09%, 3.38%, and 3.73%, respectively.

(3) Estimating sonic logs

(a) Theory

A sonic well log measurement is the time taken by the acoustic wave to travel through the formation and return back to the receiver (called transit time), which is a measure of slowness within the formation. This transit time ($\Delta t_m = t_f - t_n$), typically reported in the units of $\mu\text{s}/\text{ft}$, is the difference between the times acquired at two receivers (t_n and t_f) and is used to compute the compressional wave (P-wave) velocity (V_p) as follows:

$$V_p \left(\frac{ft}{s} \right) = \frac{10^6}{\Delta t_m} \quad (26)$$

Sonic logs play an important role in formation evaluation of unconventional reservoirs, which include modeling elastic properties of the rock that allow generating stress data to design hydraulic fracturing treatment, optimize well placement, evaluate wellbore stability, evaluate sand production, etc.

(b) Application

The ANN model was trained using the following 5 drilling parameters (Hadi and Nygaard, 2021): ROP, true vertical depth (TVD), rotation per minute (RPM), WOB, and TRQ.

The trained ANN model for travel time denoted as DT (with $n = 5$ input features and single hidden layer with $m = 3$ neurons; b_1 is the bias between input and hidden layers, and b_2 is the bias between hidden and output layers) was represented in the form of a mathematical function based on its weights (w_{1i} are the neuron weights between the input and hidden layers; w_{2i} are the neuron weights between the hidden and output layers;), transfer function (tangent-sigmoid function), and b as follows (Hadi and Nygaard, 2021):

$$DT = \sum_{i=1}^N \frac{2w_{2i}}{1 + \exp \left[-2 \sum_{i=1}^{n=5} (w_{1i,1}x_i + b_{1i}) \right]} \quad (27)$$

The numerical values of the weights and biases of the optimized ANN depicted by Eq. (27) are provided in Table A-5. The ANN model was trained and validated using well logs from one of the Iraqi oil fields (Fig. A-21), where the

R2 and root mean squared error of the DT estimated using the optimized ANN model for the training and validation datasets were (0.91, 3.27) and (0.90, 3.38), respectively. The DT estimated via optimized ANN model was validated on another carbonate formation of interest (Fig. A-22), which closely resembled the measured DT.

2.6 Identification and characterization of fracture patterns

(1) Theory

Advanced flow meters (e.g., Coriolis type flow meter) installed between the mud pumps and the mud returns flow line enable accurate flow monitoring during drilling operations. The real-time monitoring of micro mud flow in the formation via their differential can be used to characterize fracture patterns based on its loss signatures as shown in Fig. 9 (Chiniwala et al., 2018). This mud flow loss is also called 'Delta Flow', which is the change in flow out and flow in mud rate. The impact of flow variations in Delta Flow due to surface drilling operations are removed with the help of drilling parameters like stand pipe pressure, TRQ, weight on bit, and rotation per minute.

Different types of fractures can be characterized using the Delta Flow as follows:

- 1) Natural open fractures: The flow sensor continues to show a decrease in the Delta Flow volume until the mud penetrating the fracture gradually plugs the fracture and the Delta Flow volume returns to the baseline, which indicates no loss in mud with time.
- 2) Induced fractures: The Delta Flow volume shows a sharp fall in its value, followed by an immediate recovery of the lost Delta Flow volume.
- 3) Micro-fractures or matrix permeability: The Delta Flow volume shows a gradual decrease in its value until the drilling bit has moved past the zone of micro-fractures or matrix permeability. The Delta Flow can detect very fine micro-fractures that can not be seen with the wireline image logs (Dashti et al., 2021).
- 4) Cavern or large-aperture fractures: The Delta Flow volume shows a high and sudden decrease, with no recovery and return to the baseline.

(2) Application

The Delta Flow 'signatures' have been used successfully to detect fractures in the Anadarko Basin (U.S.) and in a basin in the Middle East. examples from four different areas in an exploratory well located in West Kuwait region where the Delta Flow signatures accurately predicted the presence of open natural fractures, matrix permeability, and induced fractures (Fig. A-23). The Delta Flow signatures that characterized the fractures in each of the 4 different regions were confirmed via core inspection and image log interpretation.

3. Key learnings from current state of the art

The 4 key learnings from current state of the art in real-time formation evaluation are related to: addressing the uncertainties in porosity and geochemical analysis, minimum

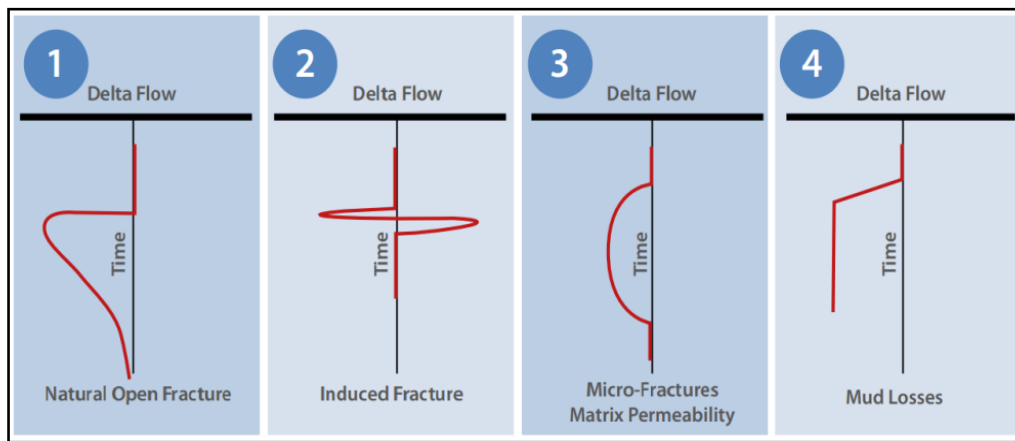


Fig. 9. Delta Flow signatures and the corresponding fracture characterization (Chiniwala et al., 2018).

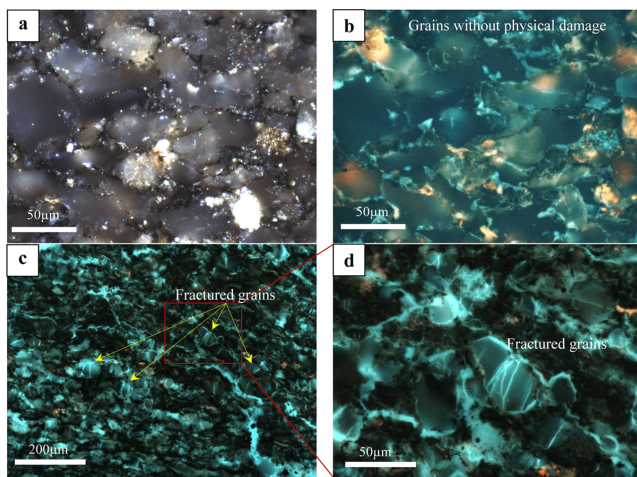


Fig. 10. Photomicrographs of ARcutt and ARcore samples (Sanei et al., 2020). Images exhibit widespread occurrence of micro-fractures in the silt grains of the ARcutt (c and d), whereas the ARcore samples (a and b) show no such physical deformation (Sanei et al., 2020).

cutting size for reliable NMR data, sweet spot identification via trapped fluid analysis, and power and network considerations for real-time analysis, respectively. These key learnings are discussed in detail as follows:

3.1 Addressing the uncertainties in porosity and geochemical analysis

Although drill cuttings have significant value as data, they are also likely to be relatively more prone to issues that can add uncertainties in the analysis, which include issues like contamination with drilling mud, physical deformations, and lack of geological representativeness. Therefore, appropriate measures must be taken to ensure suitability of the drill cutting samples for their application in wide range of analysis as discussed earlier in this study.

3.1.1 Uncertainty in porosity

Porosity measured from drill cuttings can often include uncertainties, such as artificial deformation of pore space (e.g.,

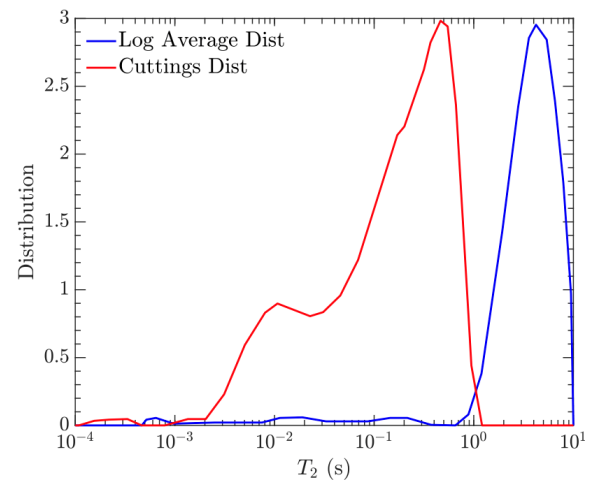


Fig. 11. Distributions of T_2 relaxation time obtained from NMR measurements on cleaned and sieved cuttings (Singer et al., 2021).

induced micro-fractures) due to stresses exerted by the drill bits (Solano et al., 2012; Althaus et al., 2020; Sanei et al., 2020). Photomicrographs of samples (from Canadian Montney tight gas) shown in Fig. 10 exhibit widespread occurrence of drilling-induced micro-fractures in the silt grains of the as-received cuttings (ARcutt) (Figs. 10(c) and 10(d)) compared to the as-received core (ARcore) samples (Figs. 10(a) and 10(b)) that show no such physical deformation.

Additionally, NMR and mercury intrusion capillary pressure (MICP) measurements performed on solvent-cleaned cuttings (SCcutt) and solvent-cleaned core (SCcore) samples from the same formation exhibit the consistent presence of larger pore diameters in SCcutt than the SCcore samples, as shown in Fig. 12, which further verifies the widespread occurrence of drilling-induced micro-fractures in drill cuttings (Sanei et al., 2020). Data with higher T_2 relaxation time indicates larger pore diameters compared to data with lower T_2 relaxation times. This significant variation in distributions of pore sizes from drill cuttings (obtained using T_2 relaxation time from NMR measurements) and the intact formation (obtained using T_2 relaxation time from LWD NMR log) can also be confirmed by another study (Singer et al., 2021) as shown in Fig. 11. To

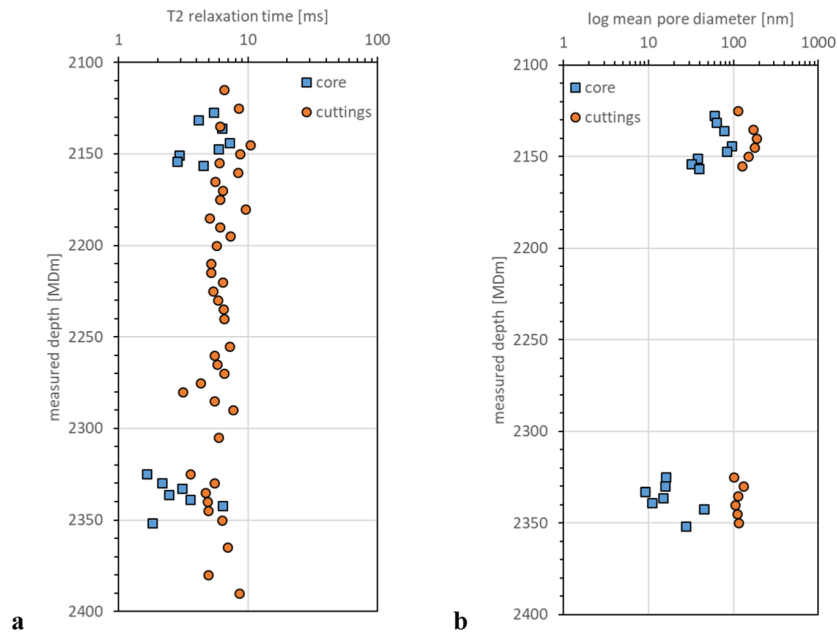


Fig. 12. Depth versus (a) T_2 relaxation time obtained from NMR measurements on solvent-cleaned cuttings and solvent-cleaned core samples, and (b) logarithmic of mean pore throat diameters obtained using MICP measurements on SCcutt and SCcore samples (Sanei et al., 2020).

ensure the porosity measured using drill cuttings are reliable and free of uncertainties, it should be compared with the other data that are free from such uncertainties, such as core samples and/or well-logs.

3.1.2 Uncertainty in geochemical analysis

Microscopic study of the drill cuttings (from Canadian Montney tight gas) as shown in Fig. 13 (Sanei et al., 2020) exhibited three major sources of contamination, which are identified as cavings (organic and inorganic matter) from overlying formations, clay-like matter from drilling mud, and volatile, oil-based invert emulsion drilling fluids, respectively. It is hypothesized (Sanei et al., 2020) that these contaminations impact the bulk geochemistry of the cutting samples.

3.2 Minimum cutting size for reliable NMR data

Integrity of pore structure is mainly affected by cutting sizes and the shear induced rock matrix distortion, which varies by rock type and grain size. Suitability of using cuttings to derive NMR petrophysical properties, such as porosity and bound volume index (BVI), is summarized in Table 2 (Singer et al., 2021), where OBM is oil-based mud and WBM is water-based mud.

3.3 Sweet spot identification via trapped fluid analysis

One of the least-focused part about drill cuttings analysis is the analysis of trapped fluids in drill cuttings. Trapped fluid analysis can aid in inferring sweet spots through characterization of the distribution and abundance of encapsulated fluids, besides providing other quantitative data about the formation fluids, such as hydrocarbon composition, GOR, API gravity,

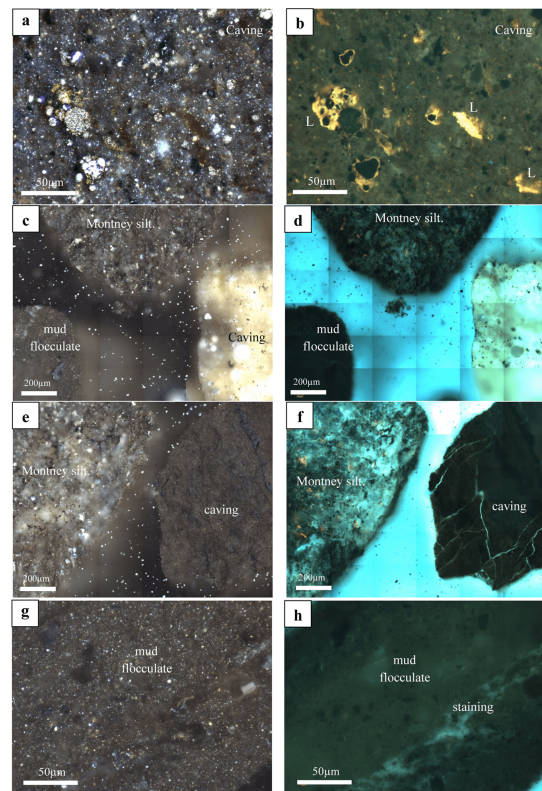
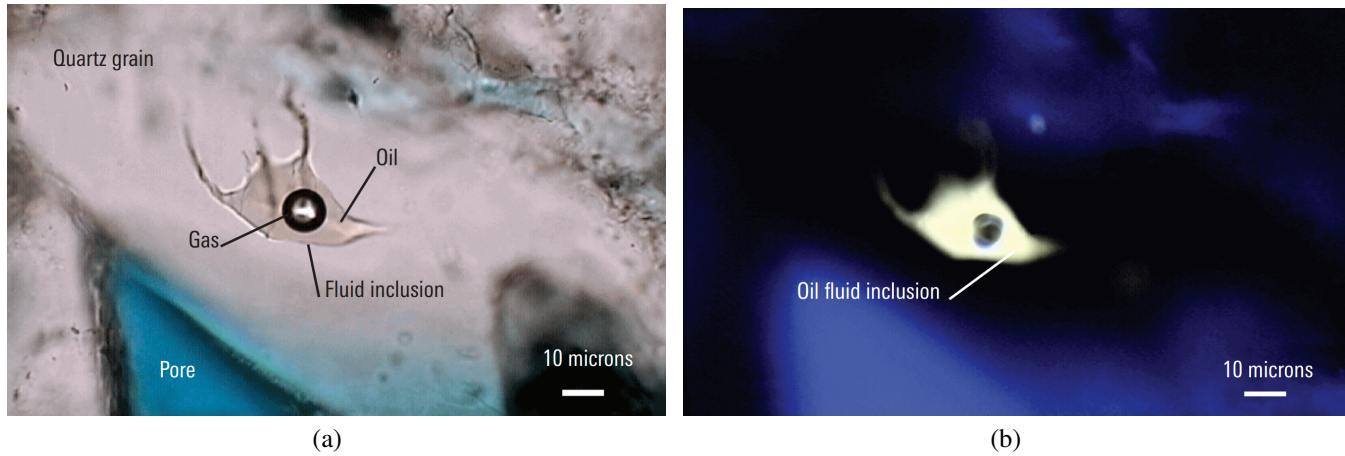


Fig. 13. Photomicrographs of ARcutt exhibit three major sources of contamination, which are identified as i) cavings (organic and inorganic matter) from overlying formations, ii) clay-like matter from drilling mud, and iii) volatile, oil-based invert emulsion drilling fluids. Images on the left column show results of reflected light organic petrography, and images on the right column show the same view in fluorescence light (Sanei et al., 2020).

Table 2. Summary of suitability of cuttings for NMR-derived formation evaluation (Singer et al., 2021).

Lithology	Minimum cutting size (mm)	Porosity	BVI	In OBM	In WBM
Carbonate	0.875	No	No	No	No
Carbonate	2.0	Yes	No	No	Yes
Sandstone	0.875	No	Yes	No	Yes
Sandstone	2.0	Yes	Yes	No	Yes

**Fig. 14.** (a) Trapped fluids in a sandstone thin section, and (b) same thin section under UV light (Schlumberger, 2021).

saturation state of hydrocarbon (HC) fluid, and salinities that can be useful in estimating irreducible water saturation (Swir). Direct quadrupole mass spectrometry allows ionization, isolation, detection, and monitoring of hydrocarbons to distinguish volatile organic species (C1-C13) and inorganic volatiles (CO₂, H₂S, He) (Schlumberger, 2021). Usually, 3 types of data are collected to analyze trapped fluid (Welker et al., 2016), as follows:

- 1) Homogenization temperature (Th) of aqueous and petroleum inclusions: It represents the minimum encapsulation (trapping) temperature of the fluid that can be used to estimate cementation temperatures, emplacement temperatures of hydrocarbon fluids, and maximum burial temperature.
- 2) Final melting temperatures (Tm) of aqueous inclusions: It can be used to determine the total salinity of trapped aqueous fluids that can be further used to estimate water saturation.
- 3) API gravity of liquid petroleum inclusions: It provides an indication of petroleum type and quality, especially when combined with Th data. API gravity of petroleum inclusions can be quantified based on fluorescence color that can be resolved optically (Fig. 14), with a total range of 21° to 48° API.

3.4 Power and network considerations for real-time analysis

An important element to enable real-time analysis of drill cuttings is the power and network consideration for the

devices used in measurements, computations, data reporting, and remote operations, typically referred to as the internet-of-things devices. Six important parameters in required to enable real-time analysis of drill cuttings at the well-site from power and network consideration are: the rate at which data is transmitted, the range over which devices can communicate with each other, power consumed by the devices, scalability, network security, and cost. The tools and devices used at the well-site are typically battery-operated and are required to run for as long as possible with minimum power consumption, which is generally addressed by low-power embedded systems. Another fundamental concept relevant to the power and network considerations is the frequency limit of the ISM (Industrial, Scientific and Medical) radio band, which varies between 6.765 MHz to 246 GHz based on its type (e.g., regional, worldwide). Oilfield applications that use SCADA (supervisory control and data acquisition) to transmit the data are typically deployed using 400 MHz and 900 MHz ISM band frequency, but they are not an ideal solution to transmit data like live video streaming that require high throughput. Live video data can be transmitted either using high throughput ISM band (e.g., 5 GHz, 6E GHz) that enable live video streaming (constant polling), or using cellular modems that can be costly depending on the data limits.

4. Conclusions

4.1 Current situation

Cuttings analysis for formation evaluation has been used for the past 50 years, but it relied on manual inspection

with specialized skills, which led to a slow and tedious process. However, advancements in Industry 4.0 technologies can now enable automated real-time formation evaluation via cuttings and drilling data analysis. Automation and data-driven models are leading to tangible commercial and environmental successes in the oil and gas industry, with successes related to smart drilling, faster completion techniques, and improved reservoir management. However, implementation of such techniques has been slow and not as prevalent in formation evaluation, which still mostly relies on traditional methods that are slow and costly.

4.2 Limitation

It is clear that real-time formation evaluation via cuttings and drilling data analysis directly benefits reservoir characterization as discussed earlier, but its current use is mostly limited to the task of lithology and rock type identification to support drilling and lateral placement. Reservoir characterization is essential to build up a geological model of the reservoir, which is traditionally a slow process, so its traditional use is limited to reservoir simulations. The state-of-the-art techniques reviewed in this paper can predict parameters relevant to reservoir and completion quality, which can enable rapid development of the geological and geomechanical models in near real-time, compared to the limited analysis for lithology and rock type identification that is currently the practice.

4.3 Prospects

Automated real-time formation evaluation can enable taking more robust real-time decisions via remote operation and collaboration between multiple teams than what the current practices allow. This will enable reducing costs, safety-related incidents, required specialized skills, inconsistencies due to data quality issues, and ultimately aid drilling, completion, and stimulation via rapid development and integration of geological/geomechanical models into the well construction process. Field results from the well construction process of CNPC employing geology-engineering integration show significant benefits (compared to the wells constructed without integration) (Chen et al., 2022) in terms of reducing the average drilling complexity (from 18% to 4.6%) and reducing the drilling cycle (from 326 days to 257 days at 8,500 m depth). Data-driven workflows (informed and assisted by physics) have an important role in enabling improved predictions than possible through empirical/physics-based models alone by removing the underlying bias and simplifying assumptions, plus their modularity allows additional improvements through continuous updates and development of new algorithms and workflows.

Acknowledgements

The authors would like to acknowledge the support of CNPC's Beijing office (Mr. Xu Wang, Mr. Yuxin Wang, Mr. Zhenzhou Yang, Mr. Fuchen Liu).

Supplementary file

<https://doi.org/10.46690/ager.2023.04.03>

Conflict of interest

The authors declare no competing interest.

Open Access This article is distributed under the terms and conditions of the Creative Commons Attribution (CC BY-NC-ND) license, which permits unrestricted use, distribution, and reproduction in any medium, provided the original work is properly cited.

References

- Abousleiman, Y. N., Hoang, S. K., Tran, M. H. Mechanical characterization of small shale samples subjected to fluid exposure using the inclined direct shear testing device. *International Journal of Rock Mechanics and Mining Sciences*, 2010, 47(3): 355-367.
- Abousleiman, Y. N., Tran, M. H., Hoang, S. K., et al. Geomechanics field and laboratory characterization of the woodford shale: The next gas play. Paper SPE 110120 Presented at the SPE Annual Technical Conference and Exhibition, Anaheim, California, USA, 11-14 November, 2007.
- Alipour, M., Esatyana, E., Sakhaee-Pour, A., et al. Characterizing fracture toughness using machine learning. *Journal of Petroleum Science and Engineering*, 2021, 200: 108202.
- Althaus, S. M., Chen, J. H., Zhang, J. NMR measurement of porosity and density from drill cuttings of unconventional tight reservoirs. Paper SPWLA 2019-BBBBBB Presented at the SPWLA 60th Annual Logging Symposium, The Woodlands, Texas, USA, 15-19 June, 2019.
- Althaus, S. M., Chen, J. H., Zhang, J., et al. Low-field nuclear magnetic resonance methodology for analysis of drill cuttings from unconventional tight reservoirs. *Energy & Fuels*, 2020, 34(12): 15990-15994.
- Canziani, A., Paszke, A., Culurciello, E. An analysis of deep neural network models for practical applications. *ArXiv preprint*, 2017: 1605.07678.
- Chen, C., Ji, G., Wang, H., et al. Geology-engineering integration to improve drilling speed and safety in ultra-deep clastic reservoirs of the Qiluitage structural belt. *Advances in Geo-Energy Research*, 2022, 6(4): 347-356.
- Cheng, G., Guo, W. Rock images classification by using deep convolution neural network. *Journal of Physics: Conference Series*, 2017, 887(1): 012089.
- Chiniwala, B., Palakurthi, A. K., Easow, I., et al. Measurement and analysis of wellbore micro losses and rock properties while drilling: A novel approach to identification of fractures in the osage and meramec formations of anadarko basin. Paper URTEC 2896976 Presented at the SPE/AAPG/SEG Unconventional Resources Technology Conference, Houston, Texas, USA, 23-25 July, 2018.
- Dashti, J., Al-Ajmi, B., Farwan, H., et al. Identification of natural open fractures, induced fractures and matrix permeability in carbonates while drilling. Paper SPWLA 2021-0084 Presented at the SPWLA 62nd Annual Logging Symposium, Virtual Event, 15-19 May, 2021.
- Di Santo, S., Yamada, T., Bondabou, K., et al. The digital revolution in mudlogging: An innovative workflow for advanced analysis and classification of drill cuttings

- using computer vision and machine-learning. Paper SEG 2022-3750340 Presented at the SEG/AAPG International Meeting for Applied Geoscience & Energy, Houston, Texas, USA, 28 August-1 September, 2022.
- Dong, G., Chen, P. A comparative experimental study of shale indentation fragmentation mechanism at the macroscale and mesoscale. *Advances in Mechanical Engineering*, 2017, 9(8): 1-11.
- Egermann, P., Lenormand, R., Longeron, D., et al. A fast and direct method of permeability measurements on drill cuttings. *SPE Reservoir Evaluation & Engineering*, 2005, 8(4): 269-275.
- [Equinor. Cuillin: Cuttings image lithology interpretation with Neural-Networks, 2019.](#)
- Esatyana, E., Alipour, M., Sakhaee-Pour, A. Characterizing anisotropic fracture toughness of shale using nanoindentation. *SPE Reservoir Evaluation & Engineering*, 2021, 24(3): 590-602.
- Glover, K., Cui, A., Tucker, J., et al. The use of measurements made on drill cuttings to construct and apply geomechanical well profiles. Paper ARMA 2016-737 Presented at the 50th U.S. Rock Mechanics/Geomechanics Symposium, Houston, Texas, USA, 26-29 June, 2016.
- Hadi, F. A., Nygaard, R. Data driven in-situ sonic log synthesis in carbonate reservoirs. Paper ARMA 2021-1669 Presented at the 55th U.S. Rock Mechanics/Geomechanics Symposium, Virtual, 18-25 June, 2021.
- Haftani, M., Bohloli, B., Moosavi, M., et al. A new method for correlating rock strength to indentation tests. *Journal of Petroleum Science and Engineering*, 2013, 112: 24-31.
- Ismailova, L., Dochkina, V., Al Ibrahim M, et al. Automated drill cuttings size estimation. *Journal of Petroleum Science and Engineering*, 2022, 209: 109873.
- Katende, A., Rutqvist, J., Bengel, M., et al. Convergence of micro-geochemistry and micro-geomechanics towards understanding proppant shale rock interaction: A Caney shale case study in southern Oklahoma, USA. *Journal of Natural Gas Science and Engineering*, 2021, 96: 104296.
- Kathrada, M., Adillah, B. J. Visual recognition of drill cuttings lithologies using convolutional neural networks to aid reservoir characterisation. Paper SPE 196675 Presented at the SPE Reservoir Characterisation and Simulation Conference and Exhibition, Abu Dhabi, UAE, 17-19 September, 2019.
- Khoshouei, M., Bagherpour, R. Predicting the geomechanical properties of hard rocks using analysis of the acoustic and vibration signals during the drilling operation. *Geotechnical and Geological Engineering*, 2021, 39(3): 2087-2099.
- Lenormand, R., Fonta, O. Advances in measuring porosity and permeability from drill cuttings. Paper SPE 111286 Presented at the SPE/EAGE Reservoir Characterization and Simulation Conference, Abu Dhabi, UAE, 19-21 October, 2007.
- Mahmoud, A. A., Gamal, H., Mutrif, O., et al. Artificial neural networks-based equation for real-time estimation of the dynamic Young's modulus. Paper ARMA 2021-1907 Presented at the 55th U.S. Rock Mechanics/Geomechanics Symposium, Virtual, 20-23 June, 2021.
- Martogi, D., Abedi, S., Saadeh, C., et al. Mechanical properties of drill cuttings based on indentation testing and contact mechanics solutions. Paper SPE 196214 Presented at the SPE Annual Technical Conference and Exhibition, Calgary, Alberta, Canada, 30 September-2 October, 2019.
- Mohnke, O., Bartetzko, A., Ritzmann, N., et al. Integration of advanced cuttings analysis and fluid typing with NMR and acoustic logs for petrophysical log interpretation without radioactive sources. Paper SPE 183845 Presented at the SPE Middle East Oil & Gas Show and Conference, Manama, Kingdom of Bahrain, 6-9 March, 2017.
- Prioul, R., Nolen-Hoeksema, R., Loan, M., et al. Using cuttings to extract geomechanical properties along lateral wells in unconventional reservoirs. *Geophysics*, 2018, 83(3): MR167-MR185.
- Sanei, H., Ardakani, O. H., Akai, T., et al. Core versus cuttings samples for geochemical and petrophysical analysis of unconventional reservoir rocks. *Scientific Reports*, 2020, 10(1): 7920.
- [Schlumberger. Fluid Inclusion Petrography and Microthermometry, 2020.](#)
- Shi, X., Jiang, S., Wang, Z., et al. The application of drill cuttings to evaluate the fracability in unconventional shale gas resources. Paper SPE 196529 Presented at the SPE/IATMI Asia Pacific Oil & Gas Conference and Exhibition, Bali, Indonesia, 29-31 October, 2019.
- Singer, G., Flaum, M., Chen, S., et al. NMR drill cutting analysis: Methodology evaluation and operational best practices. Paper SPWLA 2021-0095 Presented at the SPWLA 62nd Annual Logging Symposium, Virtual Event, 17-20 May, 2021.
- Solano, N. A., Clarkson, C. R., Krause, F. F., et al. Drill cuttings and characterization of tight gas reservoirs-an example from the nikanassin Fm. in the deep basin of Alberta. Paper SPE 162706 Presented at the SPE Canadian Unconventional Resources Conference, Calgary, Alberta, Canada, 30 October-1 November, 2012.
- Tamaazousti, Y., François, M., Kherroubi, J. Automated identification and quantification of rock types from drill cuttings, in *SEG Technical Program Expanded Abstracts*, edited by Nedorub, O. and Swinford, B., Society of Exploration Geophysicists, Tulsa, pp. 1591-1595, 2020.
- Truong-Lam, H. S., Cho, S. J., Lee, J. D. Simultaneous in-situ macro and microscopic observation of CH₄ hydrate formation/decomposition and solubility behavior using Raman spectroscopy. *Applied Energy*, 2019, 255: 113834.
- Welker, C., Feiner, S., Lishansky, R., et al. Trapped fluid analysis of 58 wells from the SCOOP and STACK plays, Oklahoma, in *SEG Global Meeting Abstracts*, edited by Blasingame T., Rhodes S. and Sparkman, G., Unconventional Resources Technology Conference, Texas, pp. 2922-2933, 2016.
- Wittman, B., Hemenway, M., Dick, M., et al. Integration of geochemical and petrophysical measurements from drill cuttings for unconventional reservoir characterization, Converse County, Powder River Basin. Paper URTEC 2020-3290 Presented at the SPE/AAPG/SEG Unconven-

tional Resources Technology Conference, Virtual, 20-22 July, 2020.

Yamada, T., Di Santo, S. Instance segmentation of piled rock particles based on mask R-CNN. Paper IGARSS 22092014 Presented at IGARSS 2022-2022 IEEE International Geoscience and Remote Sensing Symposium,

Kuala Lumpur, Malaysia, 17-22 July, 2022.

Yang, Z., Zou, C., Gu, Z., et al. Geological characteristics and main challenges of onshore deep oil and gas development in China. *Advances in Geo-Energy Research*, 2022, 6(3): 264-266.